Suitability of simple rheological laws for the numerical simulation of dense pyroclastic flows and long-runout volcanic avalanches

Karim Kelfoun[1]

[1]   The rheology of volcanic rock avalanches and dense pyroclastic flows is complex, and it is difficult at present to constrain the physics of their processes. The problem lies in defining the most suitable parameters for simulating the behavior of these natural flows. Existing models are often based on the Coulomb rheology, sometimes with a velocity-dependent stress (e.g., Voellmy), but other laws have also been used. Here I explore the characteristics of flows, and their deposits, obtained on simplified topographies by varying source conditions and rheology. The Coulomb rheology, irrespective of whether there is a velocity-dependent stress, forms cone-shaped deposits that do not resemble those of natural long-runout events. A purely viscous or a purely turbulent flow can achieve realistic velocities and thicknesses but cannot form a deposit on slopes. The plastic rheology, with (e.g., Bingham) or without a velocity-dependent stress, is more suitable for the simulation of dense pyroclastic flows and long-runout volcanic avalanches. With this rheology, numerical flows form by pulses, which are often observed during natural flow emplacement. The flows exhibit realistic velocities and deposits of realistic thicknesses. The plastic rheology is also able to generate the frontal lobes and lateral levées which are commonly observed in the field. With the plastic rheology, levée formation occurs at the flow front due to a divergence of the driving stresses at the edges. Once formed, the levées then channel the remaining flow mass. The results should help future modelers of volcanic flows with their choice of which mechanical law corresponds best to the event they are studying.

1.   Introduction

[2]   Pyroclastic flows (PF) are fast-moving density currents composed of hot gas and rocks. They generally comprise two parts: a dense part and a dilute part [e.g., *Lacroix*, 1904; *Sparks*, 1976]. The dense part follows existing valleys; its thickness and density are thought to be close to those of the deposit and its dynamics are probably ruled by the interaction of its particles [e.g., *Sparks*, 1976; *Branney and Kokelaar*, 2002]. The dilute part of the flow is known as a pyroclastic surge or ash cloud surge. It is less confined by the topography and its dynamics are mainly governed by the gas it contains [e.g., *Valentine*, 1987]. Only the dense portion of the flow is studied here, and the abbreviation PF is used to refer to this part alone. Long-runout volcanic debris avalanches (LRA) are sudden and rapid movements of rock due to gravity, usually resulting from a collapse of the volcano flank [e.g., *Siebert*, 1984; *Voight et al.*, 1981]. LRA deposits

are several tens of meters thick and can extend to a distance of some tens of kilometers from where the collapse occurred [e.g., *Shaller*, 1991; *Hayashi and Self*, 1992].

[3]   Even though PF and LRA are triggered by very different processes, they share a number of similarities. They are both characterized by high mobility and an apparently very fluid behavior [e.g., *Sparks et al.*, 1978; *Hayashi and Self*, 1992; *Legros*, 2002]. They are both composed of polydisperse rock fragments, ranging in size from fine ashes to large blocks (in the order of one cubic meter for PF, and more than several tens of cubic meters for LRA). In both cases the deposit thickness is very small relative to the runout, and the deposits are present on a wide range of slopes (0 to ~30°). In addition they often share similar morphological features, such as raised lateral edges (levées) and a rounded front (Figure 1) [e.g., *Sparks et al.*, 1978; *Nairn and Self*, 1978; *Shaller*, 1991].

[4]   There is a real need to estimate the first order rheology of these types of flows. In terms of hazard assessment, the rheology determines the thickness, extension and the velocity of simulated flows. A poor estimation of the rheology results in a concomitantly poor estimate of endangered areas, thus rendering numerical simulation useless. For example, a poor

---

[1]Laboratoire Magmas et Volcans, CNRS, UMR 6524, IRD, Université Blaise Pascal Clermont-Ferrand II, Clermont-Ferrand, France.
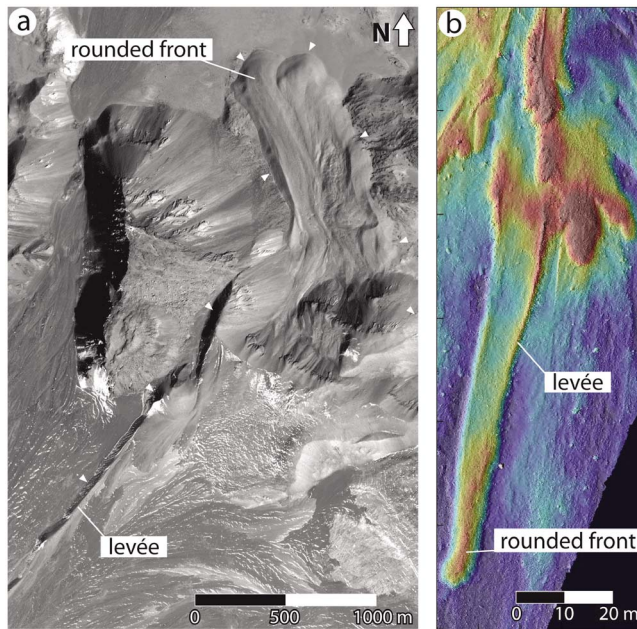
Figure 1. (a) Morphology with levées and rounded front of a debris avalanche (the ~1 km³ secondary avalanche of Socompa that formed on the toreva topography of the principal avalanche ~26 km³), Chile, 24°21′S, 68°18′W (courtesy of P. Labazuy, LMV). The white triangles indicate the deposit boundary. The scar is located 4 km to the southeast and is not visible on the image. (b) Pumice flows of Lascar volcano, Chile (23°23′20″S, 67°43′14″W). Morphology calculated by ground lidar (D. E. Jessop et al., submitted manuscript, 2011).

estimation of the velocity on natural topography will hinder the prediction of whether a flow is able to cross a given obstacle. Moreover, a calculated velocity which is too high allows the numerical flows to escape the valleys and to deposit on the interfluves, thus reducing the mass which continues to flow down the river drainage. Hazard assessment at Tungurahua volcano, for example [*Kelfoun et al.*, 2009], illustrates how an overestimation of the velocity induces an underestimation of the hazards in some sectors. From a more fundamental point of view the estimation of a correct first-order rheology of natural events is essential to test the validity of future, more complex models of the physics of such flows: even if, for computational reasons, for example, the future models only focus on small volumes of material, a test of their validity would be to reproduce and/or to explain the first-order rheology obtained by fitting simpler numerical results to field observations.

[5] Since these dense flows are constituted of rocks, grains and ashes, friction between these particles during emplacement could confer a Coulomb behavior to the whole flow. This is confirmed by the good fit between Coulomb simulations and the behavior of small rock avalanches and granular material in flumes and laboratory experiments [e.g., *Gray et al.*, 2003; *Savage and Hutter*, 1991; *Iverson et al.*, 2004]. These results explain why the Coulomb model is often used for the numerical modeling of PF and LRA, sometimes associated with a velocity-dependent term [e.g., *McEwen and Malin*, 1989; *Wadge et al.*, 1998; *Evans et al.*, 2001; *Crosta*

et al., 2004; *Sheridan et al.*, 2005; *Patra et al.*, 2005; *Procter et al.*, 2010].

[6] The angle of friction measured in PF and LRA deposits, as for many other rocks, ashes and sands, is about 30° [e.g., *Yamashita and Miyamoto*, 1993; *Miura and Yagi*, 2003; *Cecconi et al.*, 2010]. This can also be checked in the field by using the repose angle of deposits. However, if this value is used for the friction angle in numerical simulations, then the resulting simulated deposits are simply piles accumulated at the foot of the detachment scar, or close to the crater, and do not resemble either LRA or PF deposits [e.g., *Kelfoun and Druitt*, 2005; *Kelfoun et al.*, 2009]. To reach the natural runout using a simulation, the friction angle has to be lowered: 1° to 5° for LRA, 10° to 15° for pyroclastic flows [*McEwen and Malin*, 1989; *Wadge et al.*, 1998; *Evans et al.*, 2001; *Crosta et al.*, 2004; *Sheridan et al.*, 2005; *Patra et al.*, 2005; *Kelfoun and Druitt*, 2005; *Kelfoun et al.*, 2009; *Procter et al.*, 2010]. The mechanism for the reduction in friction for such complex flows has not been fully explained and various mechanisms have been evoked: fluid pressure, acoustic fluidization, mechanical fluidization, self-lubrication, dynamic fragmentation, etc. [e.g., *Davies*, 1982; *Voight et al.*, 1983; *Campbell et al.*, 1995; *Davies and McSaveney*, 1999; *Iverson and Denlinger*, 2001; *Legros*, 2002; *Collins and Melosh*, 2003].

[7] Since it is not clear which mechanism acts on the dynamics of LRA and PF to increase their runout, it is possible that these flows are subject to an overall mechanical behavior that does not follow a purely Coulomb law, i.e., with a friction angle that remains constant through time and along the whole flow. This is all the more relevant since studies have demonstrated that even glass bead flows in the laboratory do not exactly follow a Coulomb law [*Pouliquen and Forterre*, 2002]. Various rheological laws have been invoked for the simulation of natural granular flows, with the authors implicitly acknowledging that a simple Coulomb behavior is not ideal, whatever the value of friction angle used. *Heinrich et al.* [2001] and *Mangeney et al.* [2007], for example, used a friction angle that varied according to the velocity and thickness of the flows, based on the results of *Pouliquen* [1999]. Debris avalanches have sometimes been considered as viscous [*Sousa and Voight*, 1995]. Another law, commonly found in the literature for both PF and LRA, is the Bingham law (Table 1). It has been evoked to explain the typical morphology of natural deposits (bulbous front, levées), and is used in numerical simulations [e.g., *Wilson and Head*, 1981; *Voight et al.*, 1983; *Rossano et al.*, 1998; *Takarada et al.*, 1999; *Palladino and Valentine*, 1995]. This rheology is often interpreted by the authors as being related to plug flow emplacement [*Sparks*, 1976]. Based on statistical studies of LRA deposits, *Dade and Huppert* [1998] proposed a plastic rheology, i.e., the shear stress is constant whatever the thickness or the velocity of the flow. A plastic rheology can be thought of as a Bingham rheology with no viscosity. *Kelfoun and Druitt* [2005] have shown that the plastic rheology (termed the constant retarding stress) allows the morphology, lithology distribution and extension of the LRA of Socompa to be reproduced successfully. Study of Tungurahua volcano [*Kelfoun et al.*, 2009] has shown that a plastic rheology also appears to be well suited to PF simulations, even if Bingham behavior with a minor viscous response cannot be excluded.

Table 1. Mathematical Expressions of Rheological Laws Used in the Depth Average Form[a]

Name of the Law	Equation
Coulomb	$\mathbf{T} = \rho h \left(g \cos \alpha + \dfrac{\mathbf{u}^2}{r} \right) \tan \varphi_{\text{bed}} \dfrac{\mathbf{u}}{\| \mathbf{u} \|}$
One angle	$k_{\text{act/pass}} = 1$
Two angles	$k_{\text{act/pass}} = 2 \dfrac{1 \pm [1 - \cos^2 \varphi_{\text{int}}(1 + \tan^2 \varphi_{\text{bed}})]^{1/2}}{\cos^2 \varphi_{\text{int}}} - 1$
Viscous	$\mathbf{T} = 3\mu \dfrac{\mathbf{u}}{h}$
Voellmy (Coulomb + u^2 term)	$\mathbf{T} = \rho h \left(g \cos \alpha + \dfrac{\mathbf{u}^2}{r} \right) \tan \varphi_{\text{bed}} \dfrac{\mathbf{u}}{\| \mathbf{u} \|} + \xi \rho \|\mathbf{u}\| \times \mathbf{u}$
Plastic (constant retarding stress)	$\mathbf{T} = T_0 \dfrac{\mathbf{u}}{\| \mathbf{u} \|}$
Plastic + u^2 term	$\mathbf{T} = T_0 \dfrac{\mathbf{u}}{\| \mathbf{u} \|} + \xi \rho \|\mathbf{u}\| \times \mathbf{u}$
Bingham (plastic + viscous)	$\mathbf{T} = T_0 \dfrac{\mathbf{u}}{\| \mathbf{u} \|} + 3\mu \dfrac{\mathbf{u}}{h}$

[a]Terms are ρ, density; h, thickness; g, gravity; α, slope; u, depth-averaged velocity; r, slope curvature; φ_{bed}, basal friction angle; φ_{int}, internal friction angle; $k_{\text{act/pass}}$, earth pressure coefficient; μ, viscosity; T_0, yield strength; ξ, Voellmy coefficient.

[8] To improve our understanding of PF and LRA rheology, two complementary approaches can be used. The first is to define the physics of natural flows accurately. This approach is, at present, quite impossible to achieve due to the very high complexity of the natural phenomena. The second approach, which I follow here, is to determine first order empirical laws by comparing numerical results with observations and measurements of the natural events and, then, to interpret the laws and the values obtained. In the following sections I present numerical simulations of PF and LRA carried out using the various rheological laws found in the literature. I describe the typical features of each rheology, i.e., the characteristics that are common to all topographies, volumes, source conditions, etc., and explain how the simulated flows are emplaced. Finally the simulated deposits are compared with the characteristics (thickness, area of deposition, morphology) of their natural counterparts.

2. Topographies and Source Conditions Used

[9] Three topographies are used. The first topography is a simple mathematical expression that aims to capture the main characteristics of the slopes surrounding pyroclastic flows. The second topography mimics the slopes around debris avalanches. The third topography is an inclined plane

that approximates the slope surrounding the front of pyroclastic flow deposits.

2.1. Pyroclastic Flow

[10] To calculate a mathematical expression that mimics a natural slope, 4 volcanoes that have recently emitted pyroclastic flows have been chosen (Figure 2): Tungurahua (Ecuador), Merapi (Indonesia), Lascar (Chile) and Soufriere Hill (Montserrat). As can be seen on Figure 2, volcanoes that emit pyroclastic flows vary in size, but generally share the common characteristic that the slope is steep close to the crater (30–35°) and decreases progressively downslope.

[11] The slope used for the simulations has been chosen to be a mean value that aims to reproduce these characteristics. The topographic elevation, z, is given by

$$z = 2000 \times e^{-x_h/3000} - 200 \tag{1}$$

where x_h represents the horizontal distance from the crater. The PF simulations for this topography are carried out in 1D. This allows the rheological behavior to be observed under the simplest possible conditions, and is compatible with the common observation that PF are often confined to valleys (note however that the interaction with the valley walls is not taken into account in equations (6), (7), and (8)). The
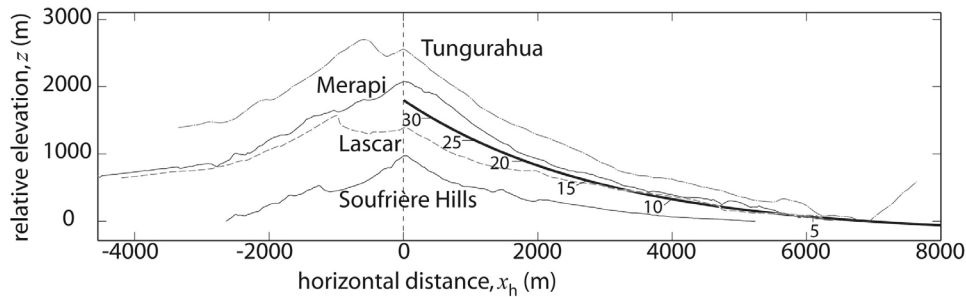

Figure 2. Four topographies of volcanoes that recently emitted pyroclastic flows. The profiles have been shifted both horizontally and vertically to place the crater rim (highest point of the slope) at the same horizontal location ($x_h = 0$) and the lowest point at $z = 0$. The thick black line is the topography used for the simulations (equation (1)). Values indicate the slope of the topography in degrees.
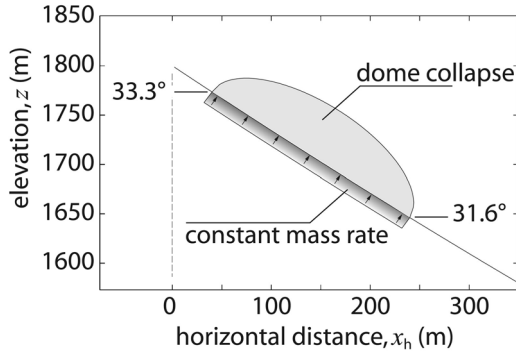
Figure 3. Initial geometry used for pyroclastic flow simulations. The mass of the dome collapse is released instantaneously. For the constant mass rate, the same mass is supplied over 60 s and 600 s.

volume of PF chosen is 10 000 m^3 per linear meter, which is compatible with the volume of deposits observed in the field, 6 to 8 km long and with a mean thickness of about 1 m [e.g., *Wilson and Head*, 1981; *Lube et al.*, 2007; *Kelfoun et al.*, 2009]. Numerical cells are 2 m long horizontally.

[12] Three source conditions are investigated. For all the simulations, the source is a zone ~236.41 m long (200 m horizontally), horizontally defined between $40 < x_h < 240$, and covering a slope between 33.3° and 31.6° (Figure 3). The first case reproduces a dome collapse. The initial thickness, calculated from the source zone normal to the slope, is given by

$$h = a\sqrt{1 - \left(\frac{x_h - 140}{100}\right)^2} \quad (2)$$

where $a \sim 53.76$ gives a volume of 10 000 m^3/m, calculated normal and parallel to the ground. The mass is released without velocity and accelerates by gravity alone. The two other cases simulate a continuous feeding of the same volume (10 000 m^3/m) over 60 s and 600 s, respectively. The same volume is introduced into each cell at each time step (the added thicknesses differ slightly since the surface of the cells changes with the slope). The velocity of each source cell is calculated from momentum conservation, the new mass being introduced without velocity. Following *Kelfoun et al.* [2009] the bulk density is assumed to be 1300 kg/m^3 for pyroclastic flows.

2.2. Long Runout Debris Avalanche

[13] In a similar manner, the profile of the topography for the LRA is obtained by fitting natural topographies of actual volcanic debris avalanches to a simple mathematical expression. The debris avalanches chosen are Shasta (USA), Socompa (Chile), Llullaillaco (Argentina) and Mount St Helens (USA). In the same way as for the pyroclastic flows above, the first topography used is a simple 1D expression (Figure 4a).

[14] The elevation of the sliding surface used for the simulation is defined by

$$z = 1500 \times e^{-x_h/10000} \quad (3)$$

The initial thickness is a 15° wedge defined by

$$h = 1000 - x_h \tan(15°) \quad (4)$$

where h is positive ($x_h < 3732$ m). The volume is a little less than 2×10^6 m^3 per linear meter. The extension of the calculation domain is 60 km and the mesh size is 10 m horizontally.

[15] However, because LRA are often emplaced onto an open topography, a 2D mathematical expression is also used. The domain of calculation is 70×70 km^2 with mesh sizes of 100×100 m^2. The slope is a function of x_h alone (horizontal along the y axis) and is also given by equation (3). The initial shape of the mass is defined by a half cone with a 15° slope:

$$h = 1000 - d \tan(15°) \quad (5)$$

where $d = \sqrt{x_h^2 + y_h^2}$, the horizontal distance from a point located at the center of the left margin ($x_h = 0$, $y_h = 0$, Figure 4b). Equation (4) equals the profile of equation (5) along the x_h axis at $y_h = 0$. The volume of the LRA is about 7.5 km^3, more than that of Mount St Helens (2.5 km^3 [*Voight et al.*, 1983]) and Llullaillaco (~2 km^3 [*Richards and Villeneuve*, 2001]), but less than that of Socompa (26 km^3 [*Wadge et al.*, 1995]) and Shasta (26 km^3 [*Crandell et al.*, 1984]). The bulk density is assumed to be 2000 kg/m^3 for debris avalanches [*Kelfoun and Druitt*, 2005].

2.3. The Flow Front in Detail

[16] To improve the observation of the morphology of the simulated flows and of the deposits, the third topography is 2D and focuses on the final 100 m of the frontal area of pyroclastic flows. The calculation domain is 110 m × 40 m, with a resolution of 10 cm. The parameters are chosen to approximate the characteristics of the pumice flow deposit of the 1993 eruption at Lascar volcano (Figure 1b). The slope is an inclined plane of 10° along the x_h axis. This planar
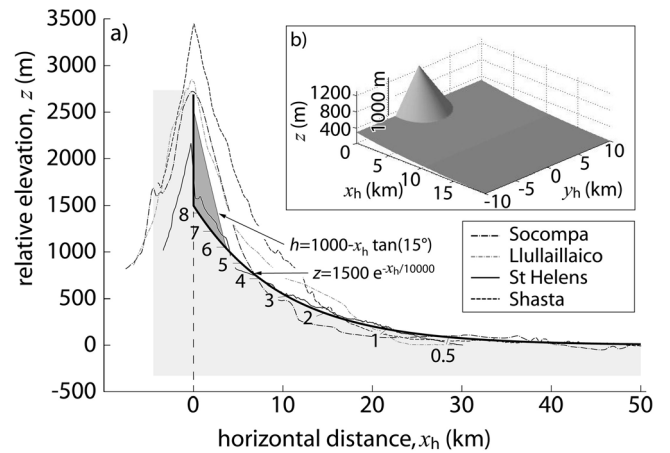

Figure 4. (a) Natural topographic profiles along the maximum extent of four debris avalanche deposits. As for Figure 2, profiles have been shifted. The pale gray area represents the topography used and the darker wedge the initial shape of the mass that will flow. (b) 3D view of the 2D topography used and of the initial shape of the mass.

Table 2. Simulations Performed[a]

	Coulomb 1 Angle: φ_{bed}	Coulomb 2 Angles: φ_{bed} φ_{int}	Voellmy φ_{bed} ξ	Plastic T_0	Plastic + $f(u^2)$ T_0 ξ
PF, 1D, dome	(1) 15°	(4) 15° 30°	(7) 5° 0.1	(10) 20 kPa	(13) 3 kPa 0.1
PF, 1D, 60 s	(2) 15°	(5) 15° 30°	(8) 5° 0.1	(11) 20 kPa	(14) 3 kPa 0.1
PF, 1D, 600 s	(3) 15°	(6) 15° 30°	(9) 5° 0.1	(12) 20 kPa	(15) 3 kPa 0.1
LRA, 1D	(16) 4°	(17) 4° 30°	(18) 4° 0.1	(19) 80 kPa	(20) 20 kPa 0.1
LRA, 2D	(21) 2°	(22) 2° 30°	(23) 2° 0.1	(24) 30 kPa	(25) 10 kPa 0.1
FF, 2D	(26) 11°	(27) 11° 30°	(28) 11° 0.1	(29) 2 kPa	(30) 2 kPa 0.1

[a]Numbers in parentheses indicate the case number, the others the rheological parameters used. Cases in italic are not presented on figures. PF, pyroclastic flow; LRA, long-runout avalanche; FF, flow front in detail.

topography has also been chosen to verify that conclusions drawn from the first cases are not due to the exponential law used. At the left side of the domain ($x = 0$), the flow is considered to have a semielliptical shape, 1.5 m high and 10 m wide (surface ~11.78 m^2), with a constant x parallel velocity of 3 m/s over a time frame of 30 s. After 30 s, the source supply ceases. The volume of the deposit is ~1057 m^3 (11.78 m^2 × 3 m/s × 30 s). These boundary conditions are assumed from the morphology of pumice flow deposits and from nondimensional comparison with granular flows in the laboratory (D. E. Jessop et al., Lidar derived morphology of the 1993 Lascar pyroclastic flow deposits, and implication for flow dynamics and rheology, submitted to *Journal of Volcanology and Geothermal Research*, 2011). The bulk density is assumed to be 1300 kg/m^3, as for the other simulations of PF. Rheological parameters are fixed to approximate the runout (~100 m) and the thickness (~1 m) of Figure 1b.

2.4. Model

[17] The numerical model is based on the depth average resolution of mass conservation (6) and momentum balance equations (equations (7) and (8)). For the simulations on a 2D topography, horizontal in the y direction, the conservation equations are as follows:

$$\frac{\partial h}{\partial t} + \frac{\partial}{\partial x}(hu) + \frac{\partial}{\partial y}(hv) = 0 \qquad (6)$$

$$\frac{\partial}{\partial t}(hu) + \frac{\partial}{\partial x}(hu^2) + \frac{\partial}{\partial y}(huv) = gh\sin\alpha$$
$$- \frac{1}{2}k_{act/pass}\frac{\partial}{\partial x}(gh^2\cos\alpha) - \frac{T_x}{\rho} \qquad (7)$$

$$\frac{\partial}{\partial t}(hv) + \frac{\partial}{\partial x}(huv) + \frac{\partial}{\partial y}(hv^2) = -\frac{1}{2}k_{act/pass}\frac{\partial}{\partial y}(gh^2) - \frac{T_y}{\rho} \quad (8)$$

The terms including v and y disappear for simulations on 1D topographies. The flow thickness is h (calculated normal to the ground), t is time, $\mathbf{u} = (u, v)$ is flow velocity along the slope, α is ground slope, ρ is the bulk density of the flow. The gravity is g (9.8 m/s^2), and x and y denote directions along the slope. Details about the equations and VolcFlow, the code that solves them, are presented by *Kelfoun and Druitt* [2005] and *Kelfoun et al.* [2009]. The variable $\mathbf{T} = (T_x, T_y)$ expresses the basal shear stress, which varies according to the rheology chosen. Table 1 gives the mathematical expressions of $\mathbf{T}$ for the different rheologies used.

[18] The Coulomb friction relates the shear stress $\mathbf{T}$ to both the normal stress at the base of the flow and the friction angle φ_{bed} between the flow and the ground (Table 1). Two models are used. In the first model, the internal friction of the flowing material, φ_{int}, implicitly equals the basal friction angle between the flow material and the ground surface, φ_{bed}, and the internal stress is considered to be isotropic ($k_{act/pass} = 1$, equations (7) and (8)). In the second model, φ_{int} differs from φ_{bed} and modifies the effect of the pressure gradient through $k_{act/pass}$, the earth pressure coefficient (equations (7) and (8)). Equations describing how $k_{act/pass}$ is calculated from φ_{bed} and φ_{int} are developed by *Iverson and Denlinger* [2001] and are given in Table 1. For all the other rheological laws used in the following sections, the internal stress in the flow is considered as being isotropic ($k_{act/pass} = 1$).

[19] Viscous rheology relates the basal shear stress to the velocity, the viscosity and the inverse of the thickness of the flow (Table 1): under the same conditions a thin flow will move more slowly than a thick one. The Voellmy law (Table 1) consists of adding to the Coulomb friction a stress which depends on the square of the velocity, incorporating a coefficient, ξ, which is used to represent the effect of turbulence and/or collisions [*Hutter and Nohguchi*, 1990; *Evans et al.*, 2001].

[20] A plastic solid (sometimes called a yield stress fluid) remains at rest while the shear stress applied to it is inferior to the yield stress T_0. Then, once movement begins, the shear stress exerted by the material is constant (i.e., it equals T_0) regardless of its thickness and velocity. If the driving stress drops back below T_0 the material decelerates and stops. A Bingham friction is one in which a viscous term is added to the plastic term (Table 1). In this case, once the yield strength, T_0, is overcome, the velocity of the flow is related to T_0, and to the viscosity, thickness and the shear stresses applied.

3. Results

[21] More than thirty simulations were performed, varying the source conditions, the topographies and the rheology. Their characteristics are listed in Table 2. Simulations incorporating viscous behavior (purely viscous, Coulomb + viscous, Bingham) are only evoked in the text, the velocity, the thickness and the deposit morphology being comparable to what is presented with the addition of a stress related to the square of the velocity (u^2 term, Table 1). For each topography and source condition, the values of the rheological parameters (e.g., basal friction angle or yield strength) are chosen to fit best to the runout of natural phenomena. This estimation,
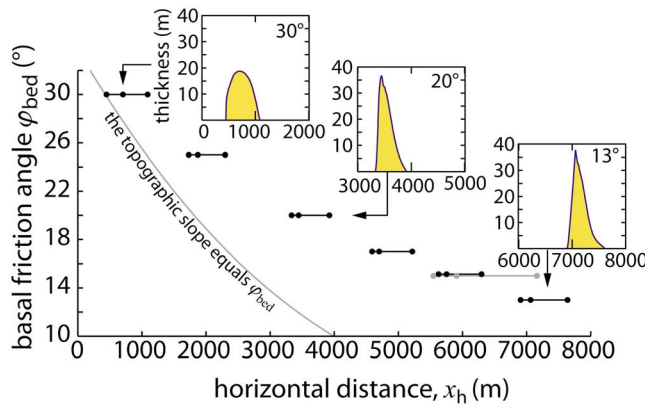
Figure 5. Distances covered by Coulomb flow deposits according to their basal friction angle. Other conditions are similar to case 2 (Table 2). Captions present the deposit geometries for φ_{bed} = 13°, 20° and 30°. The three points represent the location of the tail, the maximal thickness and the head of deposits, from left to right (volume: 10,000 m^3/m) The three gray points are obtained with a volume of 20,000 m^3/m and φ_{bed} = 15°. The gray line locates the area where the topographic slope equals the basal friction angle.

often followed by modelers who attempt to reproduce an existing event, is not based on mechanical estimations.

3.1. The Coulomb Rheology

[22] The Coulomb basal sliding is the law which is most frequently used in the simulation of PF, LRA and granular flows in the laboratory [e.g., *McEwen and Malin*, 1989; *Wadge et al.*, 1998; *Evans et al.*, 2001; *Crosta et al.*, 2004; *Sheridan et al.*, 2005; *Patra et al.*, 2005; *Pudasaini and Domnik*, 2009; *Procter et al.*, 2010]. It is thus necessary to explore its behavior in detail to determine which characteristics of long runout events it is, or is not, able to reproduce.

[23] The first simulations of PF (cases 1–3, Table 2) are carried out with an internal isotropic stress ($k_{act/pass}$ = 1, equations (7) and (8)). A basal friction angle of 15° is necessary to reach distances of ~6 km (Figure 5), commonly reached in reality by pyroclastic flows [e.g., *Ui et al.*, 1999; *Cole et al.*, 1998; *Kelfoun et al.*, 2000; *Kelfoun et al.*, 2009].

[24] For the three source conditions chosen (cases 1–3, Table 2), the behavior is rather similar. The mass leaves the

source area and accelerates where the slope of the flow surface (very close to the topographic slope) is steeper than the basal friction angle, i.e., for about 3000 m along the slope (x_h ~ 2734.5 m). Acceleration over such a distance gives the flow a velocity of nearly 100 m/s (Figure 6). Then the velocity diminishes but the high inertia allows the flow to travel about 3300 m more. The mass then accumulates over a limited distance (<1 km long, Figure 5) into a 15 to 40 m thick pile (Figure 7) with an upstream slope equaling the basal friction angle and a gentler downstream slope, due to inertia. For all the simulations done with a Coulomb material, the front stops while the tail is still flowing. The acceleration on slopes steeper than the friction angle, whatever the thickness of the flow and the shape of deposits, is typical of a material exhibiting a Coulomb basal friction [see *Pudasaini and Hutter*, 2006, and references therein]. A similar deposit shape is obtained by *Doyle et al.* [2010, Figure 9] for simulations carried out with Coulomb friction alone.

[25] The differences in behavior between the three simulations are related to the initial shape of the mass that flows. For a dome collapse (case 1), the rounded shape induces a higher initial pressure gradient than for the other simulations and thus a greater acceleration. Moreover, the center of mass is slightly higher initially than for the other cases. Thus this flow reaches the furthest runout.

[26] Simulations were also performed using two different friction angles [*Iverson and Denlinger*, 2001] (cases 4–6). As in the previous simulations, the basal friction angle is fixed at 15°, and in addition an internal friction angle of 30° is applied (the normal value for a pyroclastic deposit [e.g., *Yamashita and Miyamoto*, 1993; *Miura and Yagi*, 2003; *Cecconi et al.*, 2010]). Results obtained are very close to the previous simulation. The internal friction angle acts on $k_{act/pass}$ and thus on the stress induced by the pressure gradient (equations (7) and (8)). The stress induced by the pressure gradient being weak compared to the stress induced by the weight, because the flow is very thin over a large portion of its path, the effect of a high internal friction is consequently weak too. Deposits obtained with an internal friction angle are slightly shorter and more spread out because the internal friction opposes the convergence of material at the accumulation position (Figure 7).

[27] The density value has no influence on the emplacement of a Coulomb flow (see equations (6), (7), and (8) and
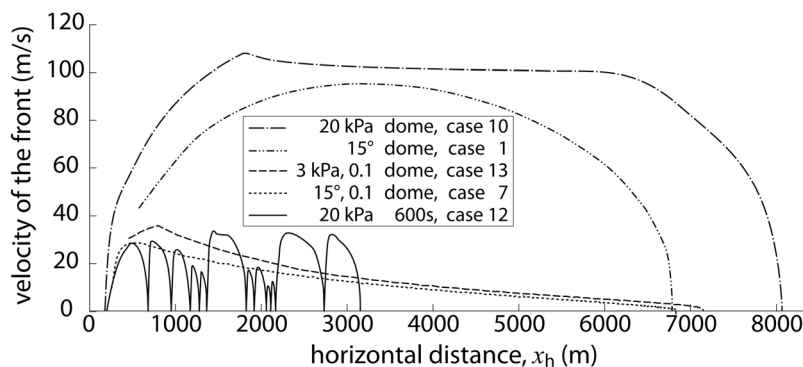

Figure 6. Velocities of the fronts of simulated pyroclastic flows for different rheologies and different source conditions.
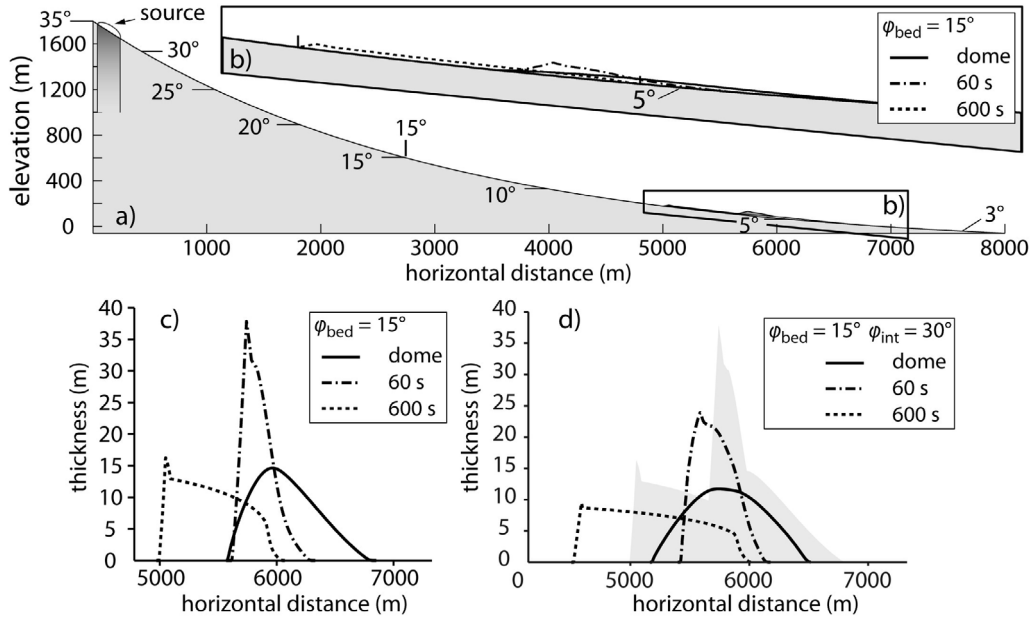
Figure 7. (a) View of the topography defined by equation (1). Coulomb deposits are restricted to a limited area (in the frame). (b) Close-up of frame in Figure 7a. (c) Deposit thicknesses obtained for the three different source conditions for a Coulomb material with $\varphi_{bed} = 15°$ and $k_{act/pass} = 1$. (d) Deposit thicknesses obtained for a Coulomb material with $\varphi_{bed} = 15°$ and $\varphi_{int} = 30°$. The gray area shows the location of the curves from Figure 7c.

Table 1) because the term ρ is canceled out. Figure 5 shows that the runout changes according to the basal friction angle but that the deposits share similar characteristics.

[28] The behavior of a Coulomb flow, as shown above, remains similar whatever the source conditions, the dimensions, the volume and the value of the basal friction angle. However, for LRA, the mean slope of the surrounding topography is generally low (Figure 4) and thus a very low basal friction angle (<5°) is required to reach the natural runout. The deposit then covers a large area compared to the area covered by the PF deposits of cases 1 to 6. For case 16 (Table 2 and Figure 8), the deposit covers about 40 km of the slope and the front forms a very thin wedge, passing progressively from 110 m to 0 m over about 30 km. The angle of this frontal wedge (<0.3°) is lower than the basal friction angle (4°) due to strong spreading caused by inertia. For case 17 (Table 2) the internal friction angle is higher than the basal friction angle, thus opposing the flow of the mass, and thereby decreasing its runout. Its effect is stronger than for the PF case because the topographic slope is gentler and the flow is thicker. The deposit for case 17 is thus emplaced closer to the source. The front also forms a thin wedge (Figure 8).

[29] For the simulation of a debris avalanche on a 2D surface (case 21), the mass flows on slopes steeper than the basal friction angle to accumulate as a pile on a limited range of slopes (Figure 9a). The effect of deposit accumulation over a large distance, observed in 1D for the LRA simulation, is less marked in 2D because the mass is free to flow around the mass which is already at rest. When the internal friction angle is higher than the basal friction angle (case 22) there is less lateral spreading of the mass (Figure 9b).

[30] For 2D simulations focused on the flow front, the flow can reach a runout of about 100 m only if the basal friction angle is slightly higher than the slope of the inclined plane. The slope being constant, the Coulomb material can be deposited over the whole domain of calculation. For higher basal friction angle values, the deposits accumulate closer to the source. For values lower than the slope, the flow accelerates continuously and no deposit forms. One particular characteristic of case 26 (Table 2) is that levées can be observed close to the source area: the thickness imposed by the boundary condition (1.5 m) is higher than the surrounding thickness of the flow (<0.4 m), since the flow is spreading rapidly. When the imposed velocity ceases, the mass of the left border accelerates due to the strong thickness gradient. This increased velocity enables the downslope deposit to remobilize the mass close to the source, forming a thinner center compared to the unaffected edges.
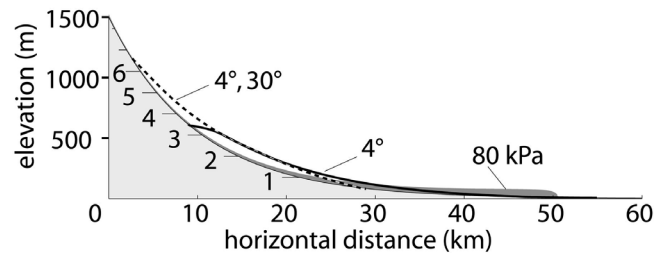

Figure 8. A 1D simulation of debris avalanches with a basal friction angle of 4° (solid line), a basal friction angle of 4° plus an internal friction angle of 30° (dotted line), and a plastic rheology of 80 kPa (shaded).
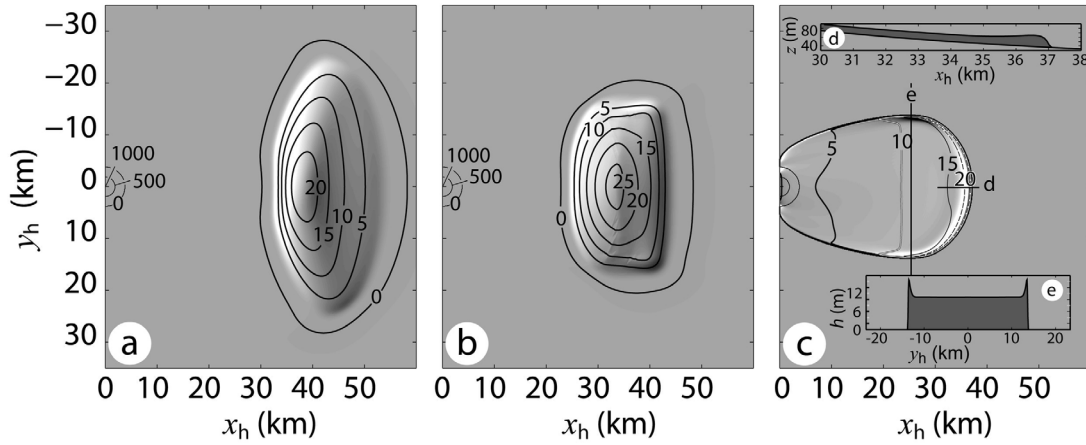
Figure 9. A 2D simulation of a debris avalanche with (a) Coulomb behavior with $\varphi_{bed} = 2°$, (b) Coulomb behavior with $\varphi_{bed} = 2°$ and $\varphi_{int} = 30°$, and (c) plastic rheology of 30 kPa. Profiles D and E are located by the rectilinear black lines. Note the formation of levées and of a well marked front. Contours indicate the deposit thickness in meters.

As will be shown in the following sections, this mechanism of levée formation differs from the mechanism exhibited by the plastic rheology.

3.2. Coulomb Rheology Plus a Velocity-Dependent Law

[31] A velocity-dependent term is often used in the literature [e.g., *McEwen and Malin*, 1989; *Wadge et al.*, 1998; *Evans et al.*, 2001], for example adding a viscous law or using a Voellmy law (Table 1). With an additional velocity-dependent stress, the friction angle must be lowered to reach the same runout as previously described. Figure 10 shows results obtained for PF simulated using a Voellmy law whose parameters are $\varphi_{bed} = 5°$ and $\xi = 0.1$ (case 7). As for the previous models, the Coulomb material begins to flow whatever the thickness. However, its velocity is reduced by the velocity-dependent term. The deposit forms a pile as previously described, but due to the lower inertia of the flow, the mass accumulates closer to the point where the slope equals the friction angle. The higher the coefficient ξ, the closer the center of mass is to this point.

[32] If Coulomb friction is combined with viscous stress, deposits form whose morphology is similar to cases 1 to 6 (purely Coulomb), but only after a very long calculation time (an infinite time is needed for all the mass to stop). This is because the resisting stress of the viscous law is proportional to the inverse of its thickness, i.e., a thin flow displaces very slowly. Note that the use of velocity-dependent laws alone (e.g., a viscous law or a law related to the square of the velocity) does not allow a deposit to form; instead the mass flows out of the calculation domain.

3.3. Plastic Rheology

[33] To reach a realistic runout of PF with the plastic rheology and dome collapse conditions (case 10), the value of the basal shear stress should be about 20 kPa (Figure 11). At the source, a shear stress of 20 kPa is very low compared to the driving stresses induced by the weight and the pressure gradient of the dome, thus the acceleration is high and the flow reaches a very high velocity of more than 100 m/s. The

constant stress rheology is very sensitive to source and geometrical conditions chosen. Decreasing the source rate reduces the flow velocity drastically, and thus the runout. A feeding time of 60 s (case 11) forms flows whose maximal velocity is 70 m/s. The flow emplaces in three pulses: at the source the mass accumulates, but remains in place until its thickness is such that the driving stress exceeds the yield stress, T_0. It then accelerates, forming a flow that thins, but in doing so it lowers the driving stress to less than T_0, thus it decelerates and stops. At the source, the mass accumulates again. When the driving stress once more exceeds the yield strength, a new pulse forms and restarts movement in the previous pulse which had come to a standstill. With the conditions in case 12 (a slow mass rate over 600 s), the flow emplaces by 12 pulses with peak velocities of the front of less than 40 m/s (Figure 6). The flow front stops after a runout of less than 3.5 km. The lower the mass rate is, the lower the velocity of the flow, and the greater the number of resultant pulses. If the mass is supplied over a duration of 600 s, a value of ~12 kPa is needed to reach a runout of ~6 km. For the equivalent runout in 2D models T_0 should have a value of only a few kPa, since the mass spreads laterally, thus
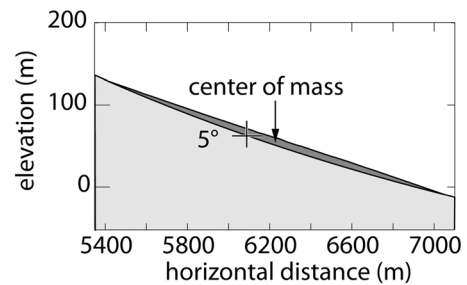

Figure 10. Deposit obtained with a Voellmy law, $\varphi_{bed} = 5°$, $\xi = 0.1$ and a dome collapse (case 7). Due to the low inertia of the material, the center of mass is close to the point where the slope equals the friction angle. Vertical exaggeration = 4.
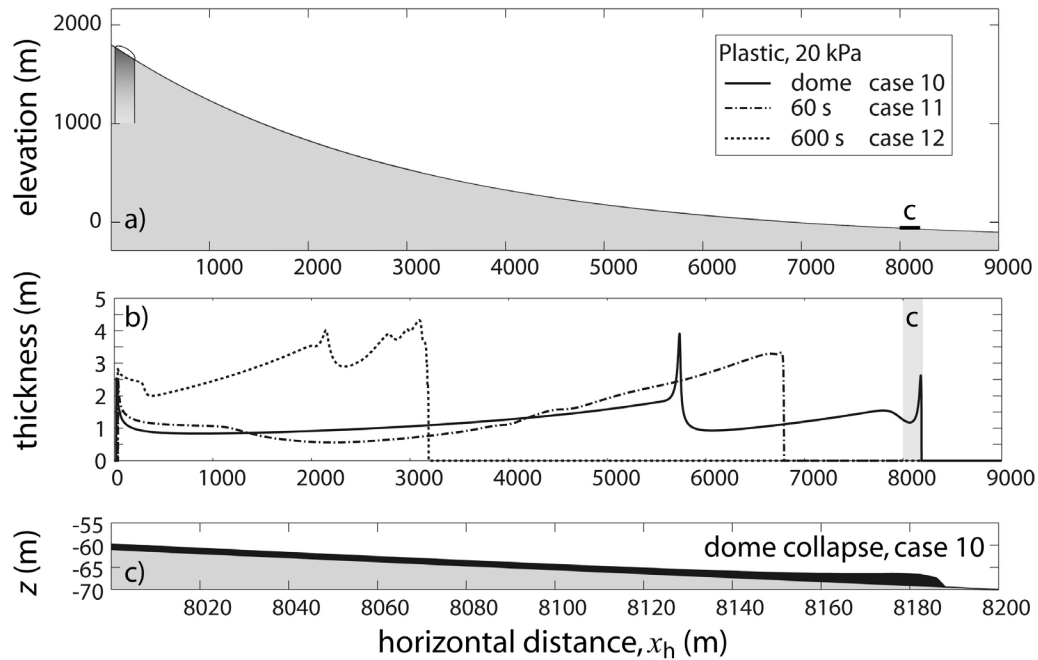
Figure 11. Simulations of PF using a plastic rheology. (a) View of the topography used and of the location of the source. The black rectangle indicates the location of Figure 11c. (b) Thickness of deposits showing a progressive increase in thickness downstream. (c) Enlargements of rectangle from Figure 8a, with the same scale for the x and z axes.

reducing the thickness of the flow and consequently the driving stress.

[34] A common characteristic of the plastic rheology (cases 10, 11, 12, 19, 24, and 29) is that the deposits cover all the areas reached by the flows and that their thickness increases where the slope angle decreases. The front of both the flow and the deposit is rounded (Figures 8, 9, 11, and 12 and Animation S1 of the auxiliary material).[1] In contrast to the Coulomb rheology, the tail of a given pulse stops while the front is still flowing and the front only stops after the source has ceased.

[35] On 2D topography, the formation of levées and a bulbous front is characteristic of this rheology (Figures 9c and 12). It occurs with all volumes, all source conditions and all topographies tested, and whatever the value of T_0: from 2 kPa for the PF in case 29 to some tens of kPa for LRA (Figures 9 and 12). This particular morphology forms at the flow front and is explained by the directions of the displacements and the driving stresses. The rounded shape of the flow front forces the mass to move laterally in this region, toward the horizontal slope of the y axis. The stress induced by the weight (oriented downslope), the stress induced by the pressure gradient and the momentum (both with a marked y parallel component) are not oriented in the same direction. At the sides of the flow front the flow spreads, thins and decelerates when the resulting driving stress is inferior to the yield strength T_0 and stops once a certain thickness is reached. This process forms static edges that channel the upstream mass (Figure 12b). Once the flow is channelized by these lateral static edges (Figure 12c), its

momentum, weight and pressure stresses, all oriented downslope, favor flow which is thinner than the lateral edges. This forms the typical levée morphology (Figure 12c). The thicknesses of the deposits and of the levées are directly related to the value of T_0 chosen.

3.4. Plastic Rheology With a Velocity-Dependent Law

[36] Simulations presented in Figure 13 are carried out with a constant shear stress of 3 kPa and a large stress related to the square of the velocity $\xi = 0.1$ (cases 13–15, Table 1). The profiles of these deposits share the same characteristics as a purely plastic flow: a progressive increase of thickness as the slope angle decreases, and a markedly rounded front. The effect of the velocity-dependent term is principally to reduce the velocity and the runout of the flow. For example, the velocity of pyroclastic flows generated by a dome collapse is less than 35 m/s (case 13). With this high value of the coefficient ξ, the shape and location of the deposit is almost independent of the source rate (Figure 13). A high coefficient ξ also tends to mask pulse formations because it smoothes velocity differences by reducing the highest velocities and also because it decreases the overall flow velocity, allowing the pulses to merge together close to the source. The lateral levées, which are related to inertia, also disappear when a high velocity-dependent stress is introduced.

4. Discussion

4.1. Coulomb Rheology

[37] Simulations carried out with the Coulomb basal friction reproduce the emplacement and the shape of sand deposits in the laboratory, sand being a material that is considered to have a Coulomb behavior at this scale [e.g.,

---

[1]Auxiliary materials are available in the HTML. doi:10.1029/2010JB007622.
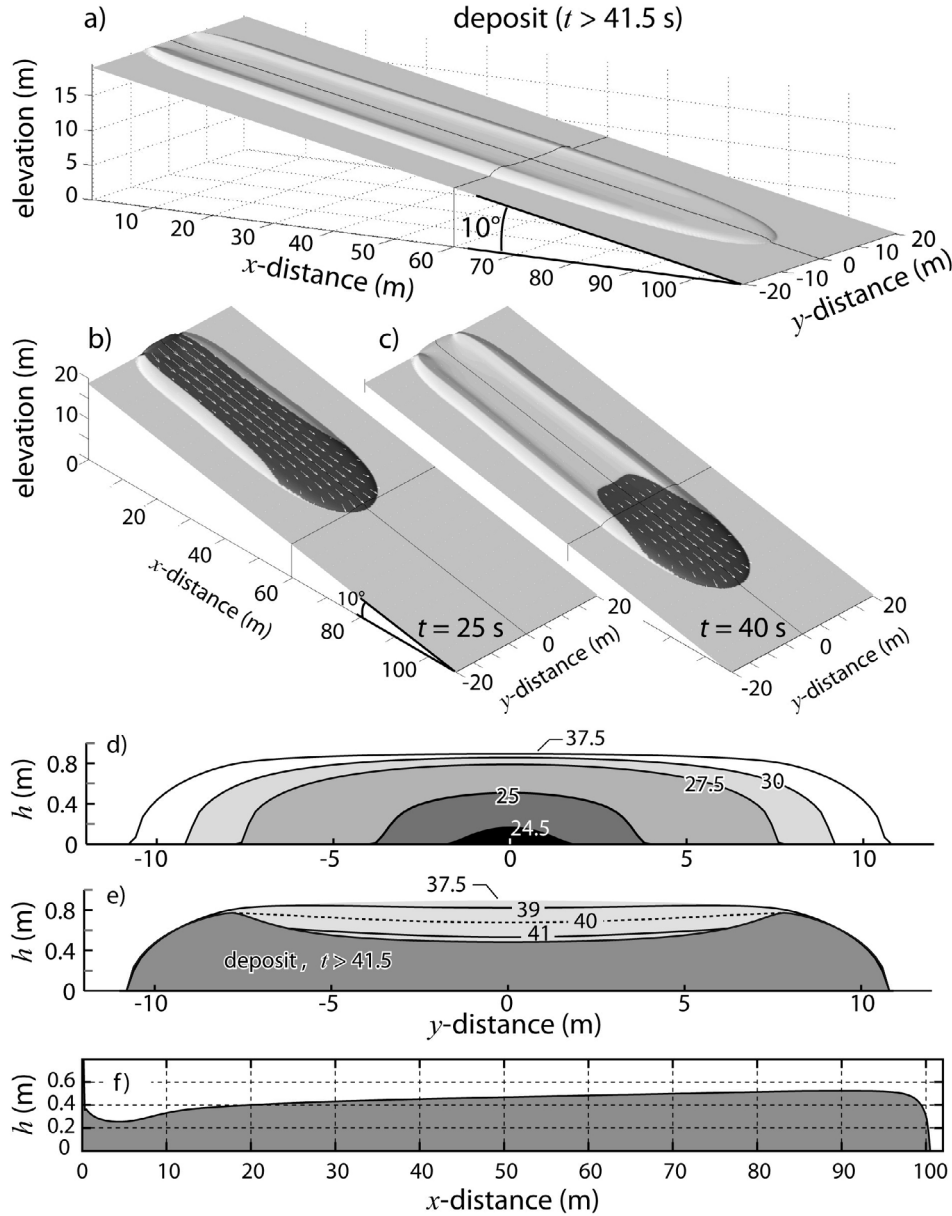
Figure 12. Simulation of a plastic flow for T = 2 kPa and a planar topography (case 29). (a) A 3D view of deposits. Black lines indicate location of Figure 12d. (b–c) The zone of displacement is shown in black. Note the formation of static edges. (d–e) Cross section of the flow at x_h = 60 m and t = 24.5, 25, 27.5, 30, 37.5, 39, 40, 41 s and the deposit. At any location covered by the flow, the thickness and the width rapidly increase with time. When the feeding rate stops, the mass of the central part drains down. The final deposit exhibits well-defined levées and a well-marked frontal lobe which is thicker than the upper parts. (f) Longitudinal section of numerical deposits (at y = 0).

Gray et al., 2003; *Pudasaini and Hutter*, 2006]. They also resemble deposits formed at the foot of cliffs by rockfalls [e.g., *Pirulli and Mangeney*, 2008, Figure 2; *Lipovsky et al.*, 2008, Figure 1].

[38] The results show, however, that the Coulomb model does not reproduce the morphology of PF and LRA deposits. Coulomb deposits only form as piles on a limited range of slopes, while their natural counterparts present sheet–like geometries if not topographically constrained, can be observed on all slopes <30°, with their thickness progres-

sively increasing as the slope decreases, and often exhibit levées and a rounded frontal lobe [e.g., *Nairn and Self*, 1978; *Shaller*, 1991]. The runout distance of a Coulomb body only increases slightly when the volume increases (Figure 5), whereas natural flows are strongly influenced by this [*Hayashi and Self*, 1992]. Finally, the friction angle that fits natural flow runouts is often less than 15° for PF and less than 4° for LRA [e.g., *McEwen and Malin*, 1989; *Heinrich et al.*, 2001; *Sheridan et al.*, 2005; *Kelfoun and Druitt*, 2005; *Kelfoun et al.*, 2009]. With such a low value for
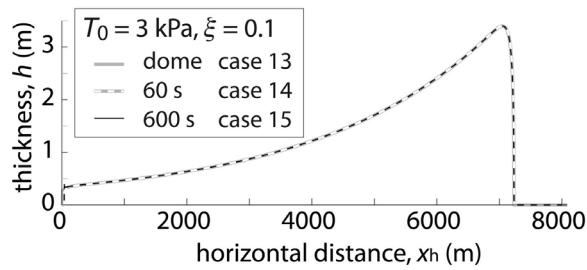
Figure 13. Deposits obtained with a plastic rheology and a term related to the square of the velocity (T_0 = 3 kPa, ξ = 0.1). The three curves obtained by varying the source conditions (case 13–15) are nearly overlapping.

the basal friction angle, the mass that accelerates on slopes steeper than the friction angle may accelerate over several kilometers, particularly for PF emitted at the summit crater. This can induce unrealistic velocities, of around 100 m/s, on intermediate slopes even for small-volume PF ($<10^6$ m^3). If used on a natural topography, the high velocity of simulated flows allows them to escape out of the drainage channels and to affect the interfluves, whereas in the field they are channelized, which makes it questionable to use the Coulomb model for PF simulation and, consequently, for hazard assessment of PF. Adding a velocity-dependent term allows more realistic velocities to be obtained, but still forms deposits with unrealistic morphologies for long-runout events.

4.2. Plastic Rheology

[39] Characteristics of deposits obtained using a plastic rheology resemble the natural long-runout deposits in the following features. First, they form well-defined levées and a rounded, bulbous frontal lobe, as often observed in the field (Figures 1, 9, and 12). Second, the plastic rheology forms sheet-like deposits on all the slopes, with the thickness increasing downslope. Note that the absence of levées on any natural deposit cannot be automatically used to reject the plastic model. According to the results, the levées form only on open topographies. They cannot be observed if the flow is confined, or on gentle slopes where inertia is low.

[40] The pulses produced by the model resemble the pulses which are often observed during real PF emplacement [e.g., *Schwarzkopf et al.*, 2005; *Kelfoun et al.*, 2009], and lead to lobes comparable to those observed on deposits (Figure 1). However, to my knowledge, it is impossible from field observation to determine that pulses are linked to the rheology of the flows or to variations in source conditions.

[41] For the simulation of PF where there is a high rate of mass release onto steep slopes, (case 10, dome collapse), the velocity obtained with the plastic rheology is too high to be compatible with any natural examples of observed velocity. PF reach a velocity of 100 m/s, which is unrealistic for this kind of flow [e.g., *Hoblitt*, 1986; *Yamamoto et al.*, 1993; *Cole et al.*, 1998; *Kelfoun et al.*, 2000; *Jolly et al.*, 2002]. Two explanations can be envisaged. It is possible that a velocity-dependent term really affects the rheology of LRA and PF, for example due to particle collisions or turbulence. An alternative explanation is that this term may be an artifact

linked to the incapacity of the existing numerical models to simulate the initial stage of rock dismantling during dome collapse and LRA simulations. Strong frictional forces might be present during the dismantling stage and could have a strong influence in reducing the initial velocity of the flow. The velocity-dependent term is correspondingly high since the velocity is high. It could then artificially reproduce a similar effect because the highest velocities are located close to the source. For the simulation of the pyroclastic flows of Tungurahua, for which the mass rate was relatively low (~0.15 m^3/s for each square meter of the source area) [*Kelfoun et al.*, 2009], and of the debris avalanche of Socompa where the basal slope was gentle (about 13°) [*Kelfoun and Druitt*, 2005], the velocity-dependent term does not exist or is small enough to be undetectable. Quantification of this velocity-related stress is difficult without very accurate measurement of the flow rates, volumes and velocities of natural flows.

[42] The results show that some mechanisms that occur in the dynamics of PF and LRA modify their behavior to the extent that the plastic rheology describes their emplacement and the deposit more accurately than any other simple law. However, the plastic rheology should be considered as no more than a first order description of the rheology of long-runout granular flows. With the simple topographies used, it is not able, for example, to reproduce the small-scale structures that often characterize LRA deposit surfaces, such as hummocks. It neglects the initial stage of LRA where destabilized rocks initially behave as a Coulomb body and probably slide en masse before forming an avalanche (e.g., Mount St Helens avalanche [*Voight et al.*, 1981]). It is also able to form deposits on slopes >35° and neglects the fact that materials revert to a Coulomb behavior after, or at the end of, flow.

[43] Moreover, the plastic rheology is not explained from a mechanical point of view. It stipulates that the shear stress at the base of the flow is independent of the thickness of the flow (in contrast to the Coulomb model, for example). One explanation would be that the material constituting LRA and PF exhibits a cohesive frictionless behavior, the static angle of friction being eliminated during the flow. Other explanations for the constant stress can also be envisaged. For example, assuming that the Coulomb friction is the main stress in the flow, a constant basal friction of the flow $T = \rho g h \tan \varphi_{bed}$ can be obtained if the friction angle φ_{bed} increases as the flow thickness, h, decreases. This increase of the friction angle is present in the law used by *Mangeney et al.* [2007] and also allows them to form levées. Although speculative, several hypotheses can be envisaged to explain this inverse relationship between thickness and friction angle. Among them, the presence of resistant blocks or coherent panels in a fluidized matrix could increase the solid interaction with the ground where flows thin to a value close to that of the thickness of the blocks. It is also well known that interstitial gas (volcanic or atmospheric) acts on particles to reduce their interaction and that, for the same permeability, thin flows lose their gas more rapidly than thicker ones [e.g., *Geldart*, 1986; *Roche et al.*, 2004; *Druitt et al.*, 2007, and references therein]. Thus the friction angle increases more rapidly in thin flows relative to thick ones.

[44] A vertical structure within the flow that would induce an increase in the resisting stress from the base of the flows

Figure 14. Longitudinal section of pyroclastic flow deposits (Tungurahua, August 2006 eruption, courtesy of P. Samaniego). White arrows indicate the base of the last emplaced unit. Note the strong inverse grading.

up toward their surface might also be another explanation for the inverse relationship between thickness and friction. In thick flows, the low-friction interior in contact with the ground would permit flow even on gentle slopes, the more frictional outer part simply being rafted. As the flow thins, the influence of the more resistant part would increase. The morphological resemblance between PF and LRA deposits and lavas (lobes, levées and rounded fronts) appears to support a vertical variation of the rheology in long-runout natural flows. This concept is close to the plug flow model proposed from field observations for mudflows, debris avalanches and pyroclastic flows [e.g., *Sparks*, 1976; *Branney and Kokelaar*, 2002, and references therein]. It is compatible with detailed observations of the Socompa avalanche, which has been interpreted as a fluid-like interior surrounded by a more resistant brittle exterior [*Kelfoun et al.*, 2008]. This upward increase in the friction may be induced by the vertical variations of the flow granulometry. Deposits often present strong inverse grading: the base is composed of a matrix of fine particles, and the mean size of particles increases toward the surface. This has been observed in LRA deposits [e.g., *Shaller*, 1991, and references therein] as well as in PF deposits (Figure 14). Gas, for example, is one mechanism which is more efficient at reducing friction between finer than coarse particles. [e.g., *Geldart*, 1986]. With such a vertical structure, where the flow thins, the influence of the coarser frictional surface would induce an increase of the friction angle at the base of the flow.

5. Conclusion

[45] This article explores the behavior of flows using simple first-order rheologies for the simulation of pyroclastic flows and long runout volcanic avalanches. I carried out more than 30 simulations on simple topographies that are representative of the characteristics of natural relief. The plastic rheology reproduces, to the first order, the main morphological features of natural long-runout granular flow

deposits: levées, inverse relationship between thickness of deposits and slope, bulbous front. Future models of PF and LRA will have to reproduce a global behavior close to the plastic behavior in order to be validated and will have to explain why the plastic rheology fits the morphology of PF and LRA deposits better than the Coulomb rheology. While this question remains, as yet, unanswered, the success of the plastic rheology over the Coulomb rheology might indicate that the friction angle at the base of LRA and PF decreases depending on the thickness of the flow and cannot be considered as constant, although it is not clear which process induces this behavior. The results show, however, that for a high mass rate of material (dome collapse for example) this first-order rheology is too simple, perhaps because it does not describe the dismantling stage, or because a real velocity-dependent stress acts on fast flows. To refine this first-order rheology and improve our knowledge of its limitations, accurate field data are needed, and volcanic monitoring needs to focus on the acquisition of pyroclastic flow characteristics during their emplacement, for example volume, flow rate and velocity. In the meantime, the data available are accurate enough to state that the simple Coulomb friction is too far removed from natural deposits to be suitable for the simulation of PF and LRA. Thus, given our current state of knowledge, behavior laws based on a plastic rheology are a better alternative.

References

Branney, M. J., and P. Kokelaar (2002), *Pyroclastic Density Currents and the Sedimentation of Ignimbrites*, Geol. Soc. Mem., 27, 143 pp.

Campbell, C. S., P. W. Cleary, and M. Hopkins (1995), Large-scale landslide simulations: Global deformation, velocities, and basal friction, *J. Geophys. Res.*, 100, 8267–8283, doi:10.1029/94JB00937.

Cecconi, M., M. Scarapazzi, and G. Viggiani (2010), On the geology and the geotechnical properties of pyroclastic flow deposits of the Colli Albani, *Bull. Eng. Geol. Environ.*, 69(2), 185–206, doi:10.1007/s10064-009-0250-x.

Cole, P. D., E. S. Calder, T. H. Druitt, R. Hoblitt, R. Robertson, R. S. J. Sparks, and S. R. Young (1998), Pyroclastic flows generated by gravitational instability of the 1996–1997 lava dome of Soufrière Hills Volcano, Montserrat, *Geophys. Res. Lett.*, 25(18), 3425–3428, doi:10.1029/98GL01510.

Collins, G. S., and H. J. Melosh (2003), Acoustic fluidization and the extraordinary mobility of sturzstroms, *J. Geophys. Res.*, 108(B10), 2473, doi:10.1029/2003JB002465.

Crandell, D. R., C. D. Miller, H. X. Glicken, R. L. Christiansen, and C. G. Newhall (1984), Catastrophic debris avalanche from ancestral Mount Shasta volcano, *Calif. Geol.*, 12(3), 143–146.

Crosta, G. B., H. Chen, and C. F. Lee (2004), Replay of the 1987 Val Pola landslide, Italian Alps, *Geomorphology*, 60(1–2), 127–146, doi:10.1016/j.geomorph.2003.07.015.

Dade, W. B., and H. E. Huppert (1998), Long-runout rockfalls, *Geology*, 26, 803–806.

Davies, T. R. (1982), Spreading of rock avalanche debris by mechanical fluidization, *Rock Mech.*, 15, 9–24, doi:10.1007/BF01239474.

Davies, T. R., and M. J. McSaveney (1999), Runout of dry granular avalanches, *Can. Geotech. J.*, 36, 313–320, doi:10.1139/t98-108.

Doyle, E. E., A. J. Hogg, H. M. Mader, and R. S. J. Sparks (2010), A two-layer model for the evolution and propagation of dense and dilute regions of pyroclastic currents, *J. Volcanol. Geotherm. Res.*, 190, 365–378, doi:10.1016/j.jvolgeores.2009.12.004.

Druitt, T. H., G. Avard, G. Bruni, P. Lettieri, and F. Maez (2007), Gas retention in fine-grained pyroclastic flow materials at high temperatures, *Bull. Volcanol.*, *69*, 881–901, doi:10.1007/s00445-007-0116-7.

Evans, S. G., O. Hungr, and J. J. Clague (2001), Dynamics of the 1984 rock avalanche and associated distal debris flow on Mount Cayley, British Columbia, Canada; implications for landslide hazard assessment on dissected volcanoes, *Eng. Geol.*, *61*, 29–51, doi:10.1016/S0013-7952(00)00118-6.

Geldart, D. (1986), *Gas Fluidization Technology*, John Wiley, Hoboken, N. J.

Gray, J. M. N. T., Y. C. Tai, and S. Noelle (2003), Shock waves, dead zones and particle-free regions in rapid granular free-surface flows, *J. Fluid Mech.*, *491*, 161–181, doi:10.1017/S0022112003005317.

Hayashi, J. N., and S. Self (1992), A comparison of pyroclastic flow and debris avalanche mobility, *J. Geophys. Res.*, *97*, 9063–9071, doi:10.1029/92JB00173.

Heinrich, P., G. Boudon, J. C. Komorowski, R. S. J. Sparks, R. Herd, and B. Voight (2001), Numerical simulation of the December 1997 debris avalanche in Montserrat, Lesser Antilles, *Geophys. Res. Lett.*, *28*, 2529–2532, doi:10.1029/2001GL012968.

Hoblitt, R. P. (1986), Observations of the eruptions of July 22 and August 7, 1980, at Mount St. Helens, Washington, *U.S. Geol. Surv. Prof. Pap.*, *1335*, 1–44.

Hutter, K., and U. Nohguchi (1990), Similarity solutions for a Voellmy model of snow avalanches with finite mass, *Acta Mech.*, *82*, 99–127, doi:10.1007/BF01173741.

Iverson, R. M., and R. P. Denlinger (2001), Flow of variably fluidized granular masses across three-dimensional terrain: 1. Coulomb mixture theory, *J. Geophys. Res.*, *106*, 537–552, doi:10.1029/2000JB900329.

Iverson, R. M., M. Logan, and R. P. Denlinger (2004), Granular avalanches across irregular three-dimensional terrain: 2. Experimental tests, *J. Geophys. Res.*, *109*, F01015, doi:10.1029/2003JF000084.

Jolly, A. D., G. Thompson, and G. E. Norton (2002), Locating pyroclastic flows on Soufriere Hills volcano, Montserrat, West Indies, using amplitude signals from high dynamic range instruments, *J. Volcanol. Geotherm. Res.*, *118*, 299–317, doi:10.1016/S0377-0273(02)00299-8.

Kelfoun, K., and T. H. Druitt (2005), Numerical modeling of the emplacement of Socompa rock avalanche, Chile, *J. Geophys. Res.*, *110*, B12202, doi:10.1029/2005JB003758.

Kelfoun, K., F. Legros, and A. Gourgaud (2000), Statistical study of damaged trees related to the pyroclastic flows of November 22, 1994 at Merapi volcano (central Java, Indonesia): Relation between ash-cloud surge and block-and-ash flow, *J. Volcanol. Geotherm. Res.*, *100*, 379–393, doi:10.1016/S0377-0273(00)00147-5.

Kelfoun, K., T. H. Druitt, B. van Wyk de Vries, and M. N. Guilbaud (2008), Topographic reflection of Socompa debris avalanche, Chile, *Bull. Volcanol.*, *70*, 1169–1187, doi:10.1007/s00445-008-0201-6.

Kelfoun, K., P. Samaniego, P. Palacios, and D. Barba (2009), Is frictional behaviour suitable for pyroclastic flow simulation: Comparison with a well constrained eruption at Tungurahua volcano (Ecuador), *Bull. Volcanol.*, *71*, 1057–1075, doi:10.1007/s00445-009-0286-6.

Lacroix, A. (1904), *La Montagne Pelée et ses Eruptions* (in French), Masson et Cie, Paris.

Legros, F. (2002), The mobility of long-runout landslides, *Eng. Geol.*, *63*, 301–331.

Lipovsky, P. S., et al. (2008), The July 2007 rock and ice avalanches at Mount Steele, St. Elias Mountains, Yukon, Canada, *Landslides*, *5*, 445–455, doi:10.1007/s10346-008-0133-4.

Lube, G., S. J. Cronin, T. Platz, A. Freundt, J. N. Procter, C. Henderson, and M. F. Sheridan (2007), Flow and deposition of pyroclastic granular flows: A type example from the 1975 Ngauruhoe eruption, New Zealand, *J. Volcanol. Geotherm. Res.*, *161*, 165–186, doi:10.1016/j.jvolgeores.2006.12.003.

Mangeney, A., F. Bouchut, N. Thomas, J. P. Vilotte, and M. O. Bristeau (2007), Numerical modeling of self-channeling granular flows and of their levee-channel deposits, *J. Geophys. Res.*, *112*, F02017, doi:10.1029/2006JF000469.

McEwen, A. S., and M. C. Malin (1989), Dynamics of Mount St. Helens' 1980 pyroclastic flows, rockslide-avalanche, lahars, and blast, *J. Volcanol. Geotherm. Res.*, *37*, 205–231, doi:10.1016/0377-0273(89)90080-2.

Miura, S., and K. Yagi (2003), Mechanical behavior and particle crushing of volcanic coarse-grained soils in Japan, in *Characterisation and Engineering Properties of Natural Soils*, edited by T. S. Tan et al., pp. 1169–1202, A. A. Balkema, Lisse, Netherlands.

Nairn, I. A., and S. Self (1978), Explosive eruptions and pyroclastic avalanches from Ngauruhoe in February, 1975, *J. Volcanol. Geotherm. Res.*, *3*, 39–60, doi:10.1016/0377-0273(78)90003-3.

Palladino, D. M., and G. A. Valentine (1995), Coarse-tail vertical and lateral grading in pyroclastic flow deposits of the Latera Volcanic Complex (Vulsini, central Italy): Origin and implications for flow dynamics, *J. Volcanol. Geotherm. Res.*, *69*, 343–364, doi:10.1016/0377-0273(95)00036-4.

Patra, A. K., et al. (2005), Parallel adaptive numerical simulation of dry avalanches over natural terrain, *J. Volcanol. Geotherm. Res.*, *139*, 1–21, doi:10.1016/j.jvolgeores.2004.06.014.

Pirulli, M., and A. Mangeney (2008), Results of back-analysis of the propagation of rock avalanches as a function of the assumed rheology, *Rock Mech. Rock Eng.*, *41*(1), 59–84, doi:10.1007/s00603-007-0143-x.

Pouliquen, O. (1999), Scaling laws in granular flows down rough inclined planes, *Phys. Fluids*, *11*, 542–548, doi:10.1063/1.869928.

Pouliquen, O., and Y. Forterre (2002), Friction law for dense granular flows: Application to the motion of a mass down a rough inclined plane, *J. Fluid Mech.*, *453*, 133–151, doi:10.1017/S0022112001006796.

Procter, J. N., S. J. Cronin, T. Platz, A. Patra, K. Dalbey, M. F. Sheridan, and V. Neall (2010), Mapping block-and-ash flow hazards based on Titan 2D simulations: A case study from Mt. Taranaki, NZ, *Nat. Hazards*, *53*, 483–501, doi:10.1007/s11069-009-9440-x.

Pudasaini, S. P., and B. Domnik (2009), Energy considerations in accelerating rapid shear granular flows, *Nonlin. Processes Geophys.*, *16*, 399–407, doi:10.5194/npg-16-399-2009.

Pudasaini, S. P., and K. Hutter (2006), *Avalanche Dynamics: Dynamics of Rapid Flows of Dense Granular Avalanches*, 602 pp., Springer, New York.

Richards, J. P., and M. Villeneuve (2001), The Llullaillaco volcano, northwest Argentina: Construction by Pleistocene volcanism and destruction by sector collapse, *J. Volcanol. Geotherm. Res.*, *105*, 77–105, doi:10.1016/S0377-0273(00)00245-6.

Roche, O., M. A. Gilbertson, J. C. Phillips, and R. S. J. Sparks (2004), Experimental study of gas-fluidized granular flows with implications for pyroclastic flow emplacement, *J. Geophys. Res.*, *109*, B10201, doi:10.1029/2003JB002916.

Rossano, S., G. Mastrolorenzo, and G. De Natale (1998), Computer simulations of pyroclastic flows on Somma-Vesuvius volcano, *J. Volcanol. Geotherm. Res.*, *82*, 113–137, doi:10.1016/S0377-0273(97)00060-7.

Savage, S. B., and K. Hutter (1991), The dynamics of avalanches of granular materials from initiation to runout. Part I: Analysis, *Acta Mech.*, *86*, 201–223, doi:10.1007/BF01175958.

Schwarzkopf, L. M., H. U. Schmincke, and S. J. Cronin (2005), A conceptual model for block-and-ash flow basal avalanche transport and deposition, based on deposit architecture of 1998 and 1994 Merapi flows, *J. Volcanol. Geotherm. Res.*, *139*, 117–134, doi:10.1016/j.jvolgeores.2004.06.012.

Shaller, P. J. (1991), Analysis and implications of large Martian and terrestrial landslides, Ph.D. thesis, 583 pp., Calif. Inst. of Technol., Pasadena.

Sheridan, M. F., A. J. Stinton, A. Patra, E. B. Pitman, A. Bauer, and C. C. Nichita (2005), Evaluating Titan 2D mass-flow model using the 1963 Little Tahoma Peak avalanches, Mount Rainier, Washington, *J. Volcanol. Geotherm. Res.*, *139*, 89–102, doi:10.1016/j.jvolgeores.2004.06.011.

Siebert, L. (1984), Large volcanic debris avalanches: Characteristics of source areas, deposits, and associated eruptions, *J. Volcanol. Geotherm. Res.*, *22*, 163–197, doi:10.1016/0377-0273(84)90002-7.

Sousa, J., and B. Voight (1995), Multiple-pulsed debris avalanche emplacement at Mount St. Helens in 1980: Evidence from numerical continuum flow simulations, *J. Volcanol. Geotherm. Res.*, *66*, 227–250, doi:10.1016/0377-0273(94)00067-Q.

Sparks, R. S. J. (1976), Grain size variations in ignimbrites and implications for the transport of pyroclastic flows, *Sedimentology*, *23*, 147–188, doi:10.1111/j.1365-3091.1976.tb00045.x.

Sparks, R. S. J., L. Wilson, and G. Hulme (1978), Theoretical modeling of the generation, movement and emplacement of pyroclastic flows by column collapse, *J. Geophys. Res.*, *83*, 1727–1739, doi:10.1029/JB083iB04p01727.

Takarada, S., T. Ui, and Y. Yamamoto (1999), Depositional features and transportation mechanism of valley-filling Iwasegawa and Kaida debris avalanches, Japan, *Bull. Volcanol.*, *60*, 508–522, doi:10.1007/s004450050248.

Ui, T., N. Matsuwo, M. Sumita, and A. Fujinawa (1999), Generation of block and ash flow during the 1990–1995 eruption of Unzen Volcano, Japan, *J. Volcanol. Geotherm. Res.*, *89*, 123–137, doi:10.1016/S0377-0273(98)00128-0.

Valentine, G. A. (1987), Stratified flow in pyroclastic surges, *Bull. Volcanol.*, *49*, 616–630, doi:10.1007/BF01079967.

Voight, B., H. Glicken, R. J. Janda, and P. M. Douglas (1981), Catastrophic rockslide avalanche of May 18, in *The 1980 Eruptions of Mount St. Helens, Washington*, edited by P. W. Lipman and D. R. Mullineaux, *U.S. Geol. Surv. Prof. Pap.*, *1250*, 347–378.

Voight, B., R. Janda, H. Glicken, and P. M. Douglas (1983), Nature and mechanics of the Mount St. Helens rockslide-avalanche of 18 May 1980, *Geotechnique*, *33*, 243–273, doi:10.1680/geot.1983.33.3.243.

Wadge, G., P. W. Francis, and C. F. Ramirez (1995), The Socompa collapse and avalanche event, *J. Volcanol. Geotherm. Res.*, *66*, 309–336, doi:10.1016/0377-0273(94)00083-S.

Wadge, G., P. Jackson, S. M. Bower, A. W. Woods, and E. Calder (1998), Computer simulations of pyroclastic flows from dome collapse, *Geophys. Res. Lett.*, *25*, 3677–3680, doi:10.1029/98GL00710.

Wilson, L., and J. W. Head (1981), Morphology and rheology of pyroclastic flows and their deposits, and guidelines for future observations, in *The 1980 Eruptions of Mount St. Helens, Washington*, edited by P. W. Lipman and D. R. Mullineaux, *U.S. Geol. Surv. Prof. Pap.*, *1250*, 513–524.

Yamamoto, T., S. Takarada, and S. Suto (1993), Pyroclastic flows from the 1991 eruption of Unzen volcano, Japan, *Bull. Volcanol.*, *55*, 166–175, doi:10.1007/BF00301514.

Yamashita, S., and K. Miyamoto (1993), Model of pyroclastic flow and its numerical simulation, in *Sediment Problems: Strategies for Monitoring, Prediction and Control, IAHS Publ.*, *217*, 67–74.

K. Kelfoun, Laboratoire Magmas et Volcans, CNRS, UMR 6524, IRD, R 163, Université Blaise Pascal Clermont-Ferrand II, BP 10448, F-63000 Clermont-Ferrand, France. (K.Kelfoun@opgc.univ-bpclermont.fr)